Three-nucleon force effects in the ^{1}H($\vec{d}$, $\vec{p}\,p$)n reaction at 135 MeV/nucleon

K. Sekiguchi,[1,*] H. Sakai,[2] H. Witała,[3] W. Glöckle,[4] J. Golak,[3] K. Itoh,[5] H. Kamada,[6] T. Kawabata,[7] H. Kuboki,[1] Y. Maeda,[8] A. Nogga,[9] H. Okamura,[10] S. Sakaguchi,[7] N. Sakamoto,[1] Y. Sasamoto,[7] M. Sasano,[2] R. Skibiński,[3] K. Suda,[1] Y. Takahashi,[2] T. Uesaka,[7] T. Wakasa,[11] and K. Yako[2]

[1]*RIKEN Nishina Center, Wako, Saitama 351-0198, Japan*
[2]*Department of Physics, University of Tokyo, Bunkyo, Tokyo 113-0033, Japan*
[3]*Institute of Physics, Jagiellonian University, PL-30059 Krakow, Poland*
[4]*Institut für theoretische Physik II, Ruhr-Universität Bochum, D-44780 Bochum, Germany*
[5]*Department of Physics, Saitama University, Saitama 338-8570, Japan*
[6]*Department of Physics, Faculty of Engineering, Kyushu Institute of Technology, Kitakyushu 804-8550, Japan*
[7]*Center for Nuclear Study, University of Tokyo, Bunkyo, Tokyo 113-0033, Japan*
[8]*Faculty of Engineering, University of Miyazaki, Miyazaki 889-2192, Japan*
[9]*Forschungszentrum Jülich, Institut für Kernphysik, D-52425, Germany*
[10]*Research Center for Nuclear Physics, Osaka University, Ibaraki, Osaka 567-0047, Japan*
[11]*Department of Physics, Kyushu University, Fukuoka 812-8581, Japan*

(Received 21 November 2008; published 27 May 2009)

The deuteron to proton polarization transfer coefficients $K_{yy}^{y'}$ and $K_{y}^{y'}$ together with the deuteron analyzing powers are measured in three coplanar configurations of the deuteron-proton breakup reaction with a 135-MeV/nucleon polarized deuteron beam at the RIKEN Accelerator Research Facility. The data are compared with theoretical predictions based on exact solutions of the three-nucleon ($3N$) Faddeev equations with high-precision nucleon-nucleon (NN) forces, alone or combined with two $3N$ force (3NF) models, the 2π-exchange Tucson-Melbourne′(99) (TM′99) and Urbana IX. Large 3NF effects have been found for all the measured observables. Predicted effects are supported by the data, with the exception of the vector analyzing power A_y^d. For this observable, theory based on only NN forces is sufficient to explain the data. The behavior of the breakup analyzing powers is found to be different from the corresponding observables in elastic nucleon-deuteron scattering.

DOI: 10.1103/PhysRevC.79.054008 PACS number(s): 21.45.Ff, 21.30.−x, 24.70.+s

I. INTRODUCTION

One of the main interests in nuclear physics is understanding the forces acting between nuclear constituents. A hot topic in present few-nucleon system studies is the properties of three-nucleon forces (3NFs) that appear when more than two nucleons ($A \geqslant 3$) interact. An intensive study of 3NFs was begun after the establishment of high-precision nucleon-nucleon (NN) potentials in the 1990s, such as AV18 [1], CD-Bonn [2,3], and Nijmegen I, II, and 93 [4]. These NN potentials reproduce a rich set of NN data up to a laboratory energy of 350 MeV with very high precision (χ^2/datum $\sim$1). However, they fail to predict the correct experimental binding energies of three-nucleon ($3N$), i.e., ^{3}H and ^{3}He, and four-nucleon ($4N$), i.e., ^{4}He, bound states [5]. This is generally taken as evidence that 3NFs are required in the nuclear Hamiltonian. The commonly used 3NF models are based on an exchange of two pions between three nucleons, with the main factor in that process being a Δ-isobar excitation, initially proposed by Fujita and Miyazawa half a century ago [6]. Improvements in that picture have led to the Tucson-Melbourne (TM) [7] and the Urbana IX [8] 3NF models. It turns out that we can simultaneously achieve the correct binding energies for the $3N$ and $4N$ systems by including the TM or Urbana IX 3NFs in the nuclear Hamiltonian. Further evidence for 3NF effects have been reported for the binding energies of higher mass nuclei when stochastic techniques are applied [9–11]. The realistic NN forces fail to reproduce the measured binding energies of light nuclei with mass numbers $4 < A \leqslant 10$. The addition of the Urbana IX 3NF improves significantly the descriptions of the low-energy spectra of bound states for these nuclei. Recently, further improvements have been obtained by adding the so-called Illinois 3NFs to the nuclear Hamiltonian. These 3NFs include three-pion exchanges with the intermediate Δ-isobar excitation [12].

New impetus to the study of 3NFs has come from the chiral effective field theory approach to nuclear interactions (χPT). In that framework, consistent two-, three-, and more-nucleon forces have been derived on the same footing [13,14]. The first nonzero 3NFs appear at the next-to-next-to-leading order (NNLO) in χPT. So far, calculations have been performed up to the NNLO for the $3N$ system, providing reasonable agreement with experimental data for the $3N$ bound as well as the $3N$ unbound systems at a laboratory energy of $\leqslant$100 MeV/nucleon [15].

The results for the binding energies of light nuclei show that 3NFs provide non-negligible effects and are clearly required for an understanding of nuclear phenomena. The $3N$ scattering system is an attractive candidate for studying the detailed properties of 3NFs, such as momentum, spin, and/or isospin dependences. Nucleon-deuteron (Nd) elastic scattering and

*kimiko@ribf.riken.jp

the breakup reaction provide a rich set of spin observables and differential cross sections and, therefore, are suited to studying these dependences.

3NF effects in $3N$ scattering were identified for the first time by Witała *et al.* in 1998 [16] in the cross section minimum for Nd elastic scattering at incoming nucleon energies above 60 MeV. Since then, experimental studies of higher energy proton-deuteron (pd) and neutron-deuteron (nd) elastic scattering covering incident energies up to ≈250 MeV have been performed extensively and have provided precise data for cross sections [17–24] and spin observables, including analyzing powers [17–19,25–29], spin correlation coefficients [30,31], and polarization transfer coefficients [20,28,32]. Precise cross section data for elastic dp scattering taken at RIKEN with 135-MeV/nucleon deuterons show large disagreement between data and rigorous Faddeev calculations with modern NN forces [17–19]. Combining these NN potentials with 3NFs such as TM′99 [33] (TM′99 is a version of the TM force that is more consistent with chiral symmetry [34,35]) and Urbana IX removes this discrepancy and has allowed a good description of the measured cross sections. Applying the coupled-channel formulation based on the CD-Bonn potential with the Δ-isobar excitation, including the long-range Coulomb force, gives complementary results [36]. The influence of the Coulomb force is only visible at very forward angles; it is negligible in the cross section minimum, the most sensitive region for the 3NFs. These results are a clear signature of the 3NF effects in Nd elastic scattering. However, spin observables cannot always be explained when adding these 3NFs, indicating a defect in the spin-dependent parts of the presently used 3NF models [32].

The situation is even more interesting for kinematically complete dp breakup ($d + p \rightarrow p + p + n$) experiments at higher incoming nucleon energies. At higher energies, the breakup reaction starts to dominate the total cross section for the nd interaction, e.g., $\sigma^{\text{total}}_{\text{breakup}} \sim 2.5\sigma^{\text{total}}_{\text{elastic}}$ at 135 MeV/nucleon [37]. Contrary to elastic scattering, where transition amplitudes are integrated over the relative momentum of nucleons forming the deuteron, the exclusive breakup process projects the transition amplitude in a pointwise manner. The selectivity of breakup reactions together with its rich phase space allows one to single out kinematically complete configurations, where the observables are specially sensitive to properties of the 3NFs [37]. The existing higher energy dp breakup data consist of cross sections and tensor analyzing powers at 65 MeV/nucleon [38,39] and data focusing on the axial observables A^p_z, $C_{zz,z}$, and $C_{y,x} - C_{x,y}$ at 135 MeV/nucleon [40]. The pd breakup data at an incoming proton energy of 65 MeV consist of the cross sections and proton analyzing powers for numerous kinematically complete configurations [41–44].

In the present study, we extend our measurements of elastic dp scattering to the dp breakup reactions ($d + p \rightarrow p_1 + p_2 + n$). We first look theoretically for configurations and observables in which there are clear 3NF model dependences. The polarization transfer coefficient $K^{y'}_{yy}$ in particular coplanar configurations was found to show clear model dependences, with the TM′99 and Urbana IX 3NFs giving very different theoretical predictions. Such coplanar configurations are the laboratory angles $\theta_1 = 28^\circ, 30^\circ$, and 32° and $\theta_2 = 31^\circ$ for the first, p_1, and second, p_2, emerging protons, respectively, with a relative azimuthal angle between p_1 and $p_2(\phi_{12} \equiv \phi_1 - \phi_2)$ of $\phi_{12} = 180^\circ$. These configurations include the final state interaction geometry between the proton p_2 and the neutron [FSI(p_2n)] where their momenta are equal. In the measurement, the deuteron to proton polarization transfer coefficient $K^{y'}_y$ and the induced polarization $P^{y'}$ of the proton p_1 were simultaneously obtained. All the deuteron analyzing powers A^d_y, A_{yy}, A_{xx}, and A_{xz} were measured, for which strong sensitivities to the current 3NFs are also predicted.

In the next section, the details of the experimental arrangement are presented. Section III provides a description of the data analysis and experimental results. Section IV briefly reviews the basics of the theoretical $3N$ scattering formalism and gives a short description of the dynamical input used in this study. The experimental results are compared with the theoretical predictions in Sec. V, while Sec. VI presents a summary and conclusions.

II. EXPERIMENTAL PROCEDURE

A. Polarized deuteron beams and target

The breakup ^{1}H($\vec{d}$, $\vec{p}p$)n experiment was performed at the RIKEN Accelerator Research Facility (RARF) using the SMART (swinger and magnetic analyzer with rotator and twister) spectrograph system [45] including the focal plane polarimeter EPOL [46] (see Fig. 1). The atomic-beam-type RIKEN polarized ion source [47] provided vector and tensor polarized deuteron beams. The deuteron polarization axis was rotated by a spin rotation system Wien filter [48] prior to acceleration. It was set perpendicular to the scattering plane when measuring $K^{y'}_y$, $K^{y'}_{yy}$, A^d_y, and A_{yy}. For the A_{xx} measurement, the polarization axis was rotated into the scattering plane so that it pointed sideways, perpendicular to the beam. For the A_{xz} measurement, the spin symmetry axis was additionally rotated in the reaction plane and aligned at an angle β to the beam direction, with a typical value of $\beta = 47.0^\circ \pm 0.2^\circ$. The beam polarization was monitored by dp elastic scattering at 135 MeV/nucleon [32,49] and found to be 60–80% of the theoretical maximum value throughout the measurements. Liquid hydrogen with a thickness of 71 mg/cm^2 was employed as a hydrogen target (^{1}H) [50], and was bombarded with a beam intensity of 10–20 nA.

B. Detector arrangement

1. Detectors for the proton p_1

The protons p_1 with kinetic energies from 164 to 180 MeV were momentum analyzed by the magnetic spectrograph SMART [45] and detected at the second focal plane (FP2 in Fig. 1). The polarization of p_1 was measured with the focal plane polarimeter EPOL [46]. In the SMART system, the magnetic spectrograph was fixed to the ground, and the incident beam direction was rotated by the swinger magnet, giving a vertical reaction plane. For this experiment,

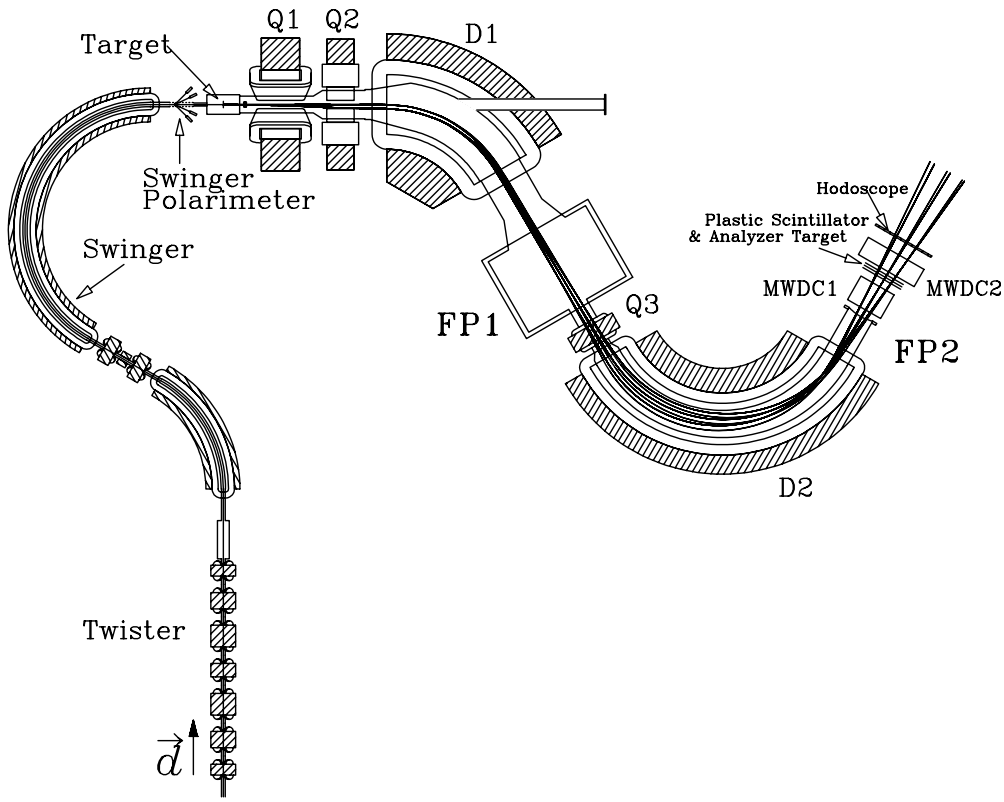

FIG. 1. Arrangement of the RIKEN spectrograph SMART. FP1 and FP2 denote the first and second focal planes, respectively. Scattered protons are momentum analyzed by the magnetic spectrograph and detected at FP2. The polarization of the scattered proton is measured with the focal plane polarimeter EPOL.

the swinger magnet was set at 31°. The collimator was set 440 mm downstream from the target. Its aperture covered the polar angles $\Delta\theta = \pm 4.2°$ and azimuthal angles $\Delta\phi = \pm 1.4°$. The solid angle was determined by binning the aperture into $\Delta\theta = \pm 1°$ and $\Delta\phi = \pm 1.4°$.

The focal plane detector system consisted of a multiwire drift chamber (MWDC1 in Fig. 2), two plastic scintillation counters (SC1 and SC2 in Fig. 2), and the polarimeter EPOL. MWDC1 was used for the reconstruction of the particle trajectory and its configuration was X-U-V-X'-U'-V'-X'-U'-V'-X-U-V. In the SMART system, the coordinate frame of a multiwire drift chamber was defined as the left-handed one as is shown in Fig. 2. The z axis referred to the central ray. The x axis was perpendicular to the z axis in the horizontal plane, and the y axis was taken as $\vec{x} \times \vec{z}$. Note this coordinate frame is different from that for the polarization observables (see Sec. III B 1). The y positions were obtained by the $U(U')$ and $V(V')$ planes, which were inclined by $+45°$ and $-45°$ with respect to the $X(X')$ planes, respectively. All the position-sensitive planes were normal to the z axis. The planes with primes were displaced by half a cell relative to the unprimed planes, which helped to solve the so-called left-right ambiguity. The cell size was 20 mm × 20 mm for the X planes and 20.5 mm × 20 mm for the U(V) planes. The plastic scintillation counters (Bicron, BC-408) of size 180 $\text{mm}^H \times 800\ \text{mm}^W \times 5\ \text{mm}^T$ (SC1 and SC2 in Fig. 2) were used to identify proton events scattered at the hydrogen target. Photomultiplier tubes (Hamamatsu, H1161) were attached at both ends of the scintillators via light guides.

The polarization of p_1 was measured by the EPOL after momentum analysis with the magnetic spectrograph. The EPOL consisted of an analyzer target, a multiwire drift chamber (MWDC2 in Fig. 2), and two sets of plastic scintillator counter hodoscopes (HOD1 and HOD2 in Fig. 2).

Polarimetry was performed through $p + \text{C}$ scattering. As a carbon analyzer target, a 5-cm-thick graphite plate was placed in front of the two plastic scintillation trigger counters SC1 and SC2. The trajectories of the scattered protons from the $p + \text{C}$ reaction were reconstructed by MWDC2. MWDC2 was located downstream of the graphite plate and had eight layers of sense wire planes with a Y_f-Y'_f-X_f-X'_f-Y_r-Y'_r-X_r-X'_r configuration. Here, subscripts f and r denote the front and rear planes, respectively. The planes with primes were, again, displaced by half a cell relative to the unprimed planes. The coordinate frame was defined as for MWDC1. The cell size was 14 × 14, 15 × 15, 14 × 14, and 16 × 16 mm for the X_f, X_r, Y_f, and Y_r planes, respectively. The number of cells was 64 for the X planes and 32 for the Y planes.

Event triggers for protons from the $p + \text{C}$ reaction on the carbon analyzer target, taken as double-scattering events, were generated from the coincidence of the signals of the SC1 and SC2 counters and the signals of the hodoscope system (HOD1 and HOD2). The angular range covered by the hodoscope system was ±20°, both vertically and

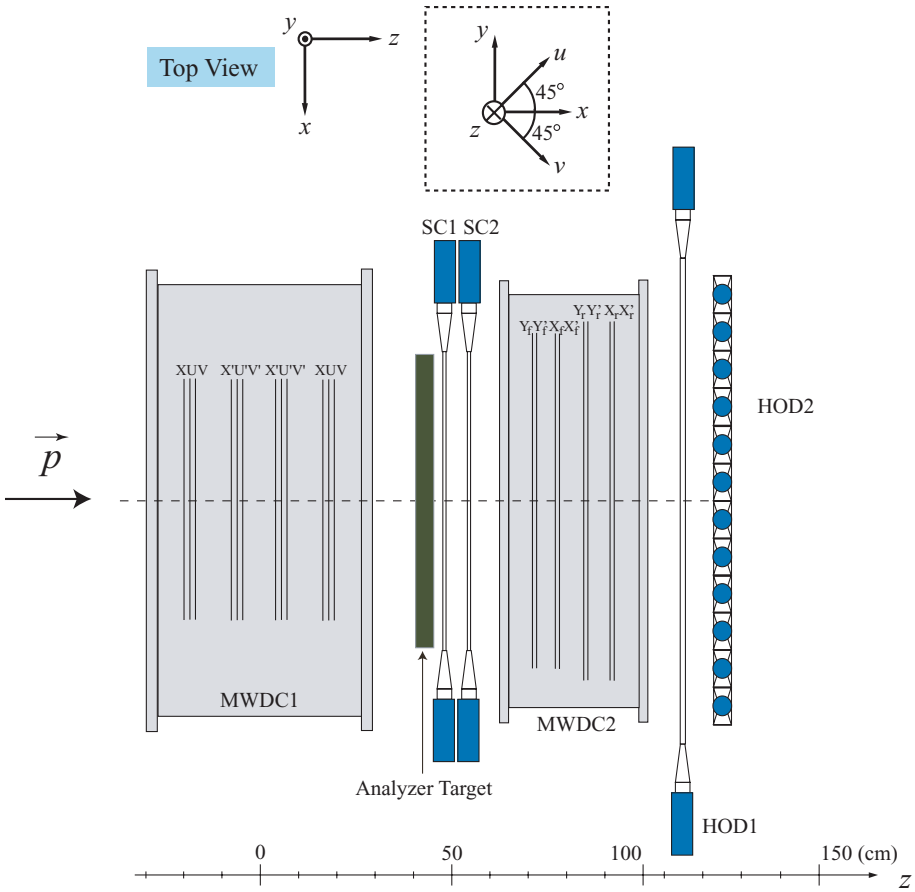

FIG. 2. (Color online) Second-focal-plane detector system including the focal plane polarimeter EPOL. The system consists of two multiwire drift chambers (MWDC1 and MWDC2), plastic scintillation trigger counters (SC1, SC2), a polarization analyzer target, and the counter hodoscope system (HOD1, HOD2). The coordinate frame used for multiwire drift chambers is shown in the upper part. The inset surrounded by a dotted line indicates the same coordinate frame viewing along the z axis.

horizontally. HOD1 consisted of nine horizontally segmented plastic scintillators, which were 1300 mm wide, 80 mm high, and 10 mm thick. HOD2 consisted of 12 vertically segmented plastic scintillators. Each HOD2 counter was 900 mm wide, 100 mm high, and 50 mm thick. Two photomultiplier tubes (Hamamatsu, H1161) were attached to both ends of each scintillation counter via light guides both for HOD1 and HOD2.

2. *Detectors for the proton p_2*

The protons p_2 were detected by the E-ΔE detectors located 390 mm downstream from the target position in the scattering chamber. The E detector was a 14-mm-diameter by 35-mm-long cylindrical NaI(Tl) scintillator mounted on a photomultiplier tube (Hamamatsu, H7415). The ΔE detector was a 2-mm-thick plastic scintillator. A 50-mm-thick brass collimator with a circular hole collimated the proton flux to the E-ΔE detectors. The aperture of the collimator hole was $\Delta\Phi = 0.8^\circ$. These detectors identified protons with energies between 30 and 75 MeV. The E detector was calibrated by measuring dp elastic scattering at several angles. The full width at half maximum (FWHM) of a peak for the elastic dp events was 3 MeV.

Event triggers for dp breakup reactions were generated by the coincidence of the signals of the E-ΔE detectors and those of the focal plane detectors. For the analyzing power measurements, the event triggers from SC1 and SC2 were used as the signals for the focal plane detectors, while the signals generated as double scattering events were used for the polarization transfer measurement.

C. Data acquisition

Data acquisition was carried out with a fast data acquisition system for the SMART spectrograph [51]. The data were accumulated in a VME memory module through a FERA bus and then DMA-transferred to a personal computer.

III. DATA ANALYSIS AND EXPERIMENTAL RESULTS

A. Selection of dp breakup events

To eliminate background and accidental coincidences, the following conditions were imposed during the analysis. First, particle identification of the protons p_1 and p_2 emerging from the dp breakup reactions was performed. The protons p_1 were selected with the plastic scintillators SC1 and SC2 at the focal plane (see Sec. II B 1). Identification of the scattered protons p_2 was performed through their energy deposits in the ΔE and E detectors shown in Fig. 3. The proton events were selected with cuts defining the particle identification as shown in the figure. Second, the "true + accidental" events and the "accidental" events were distinguished using the time-of-flight difference between the ΔE detector and the SC1 detector shown in Fig. 4. The typical S/N ratio was 1:1.

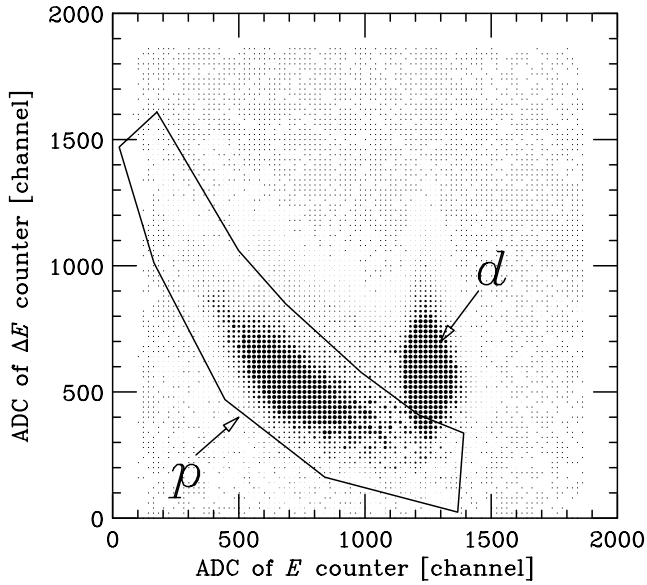

FIG. 3. Two-dimensional plot of the E-ΔE scintillation detector outputs.

By subtracting the accidental events from the true + accidental events, the spectrum of true events around a central kinematical curve of two protons p_1 and p_2 for the dp breakup reaction was obtained. An example of such a spectrum for the central positions of the proton detectors at $(\theta_1, \theta_2, \phi_{12}) = (28^\circ, 31^\circ, 180^\circ)$ is shown in Fig. 5. The kinematical curve S shown as a solid curve in the figure was calculated for the central three-body kinematics in the relativistic frame. The point at $S = 0$ was defined as that where the kinetic energies of the two protons p_1 and p_2 have equal values shown in Fig. 5. The events were projected on the central S curve and allocated to the closest S bin. As the figure shows, this configuration includes the final state interaction

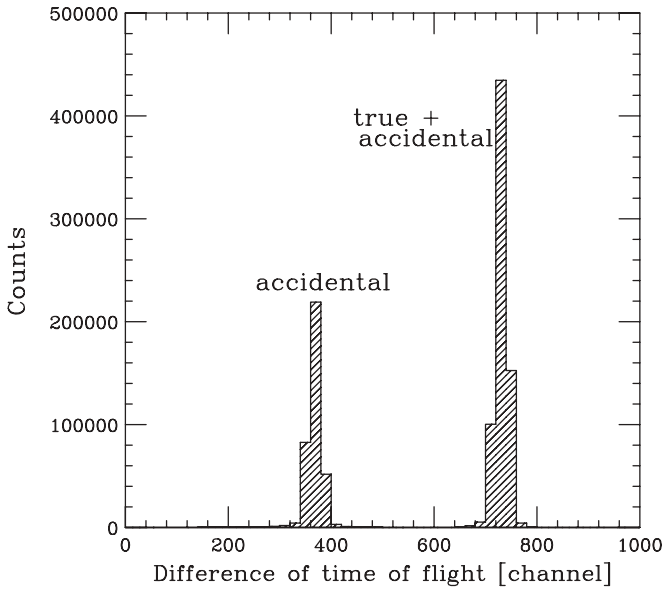

FIG. 4. Difference of the time of flight between the ΔE detector in the scattering chamber and the SC1 detector.

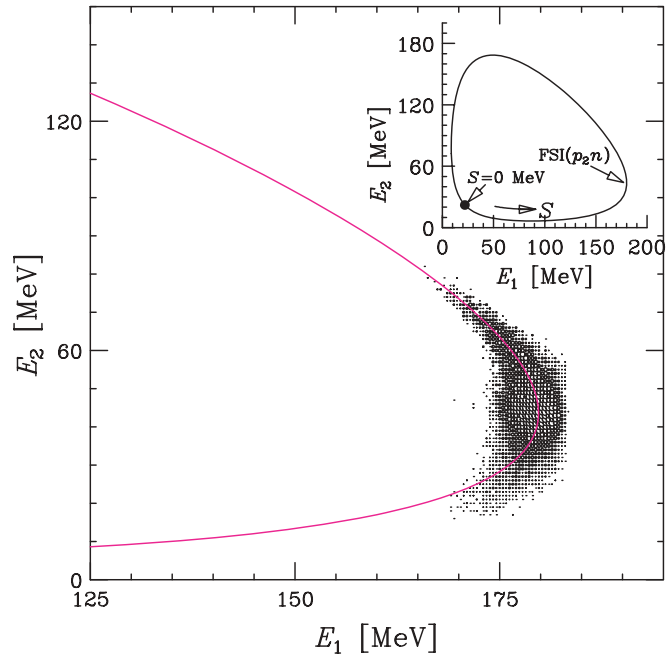

FIG. 5. (Color online) Spectrum of events for the two emerging protons p_1 and p_2 measured in a configuration with $(\theta_1, \theta_2, \phi_{12}) = (28^\circ, 31^\circ, 180^\circ)$. The solid curve is the kinematical S curve for the central three-body kinematics in the relativistic frame.

of the proton p_2 and the neutron, FSI (p_2n). The other two configurations also include the FSI (p_2n). To obtain reasonable statistical accuracy, different energy bin sizes of S were taken depending on the different observables and/or configurations: $\Delta S = 8$ MeV for A_y^d, A_{yy}, A_{xx}, and A_{xz}; $\Delta S = 18$ MeV for $K_{yy}^{y'}$ at $\theta_1 = 28^\circ$; and $\Delta S = 12$ MeV for $K_{yy}^{y'}$ at $\theta_1 = 30^\circ$ and 32°.

B. Extraction of polarization observables

1. *Coordinate frame for the polarization observables at the SMART system*

The coordinate frame for the polarization observables of the SMART system is defined according to the Madison convention [52] shown in Fig. 6. The z axis is given by the beam direction, the y axis is perpendicular to the reaction plane, and the x axis is defined by $\vec{y} \times \vec{z}$. The coordinate system (x', y', z') for the polarization of the scattered protons is rotated through the dipole magnet of the SMART spectrograph into the coordinate system at FP2 (x'', y'', z''). $\{p_{ij}\}$ in the figure are the vector or tensor deuteron beam polarizations, $p_{i'}$ denotes the polarization of the scattered protons at the target position, and $p_{i''}$ denotes the polarization of the scattered protons at FP2. The polarization $p_{y''}$ was measured with the focal plane polarimeter EPOL, and $p_{y'}$ was extracted from $p_{y''}$ and the spin precession angle χ in the dipole magnets of the spectrograph.

2. *Calibration of effective analyzing powers of the EPOL*

The effective analyzing power A_y^C of the EPOL was calibrated at a proton energy of 168 MeV. Since the polarized

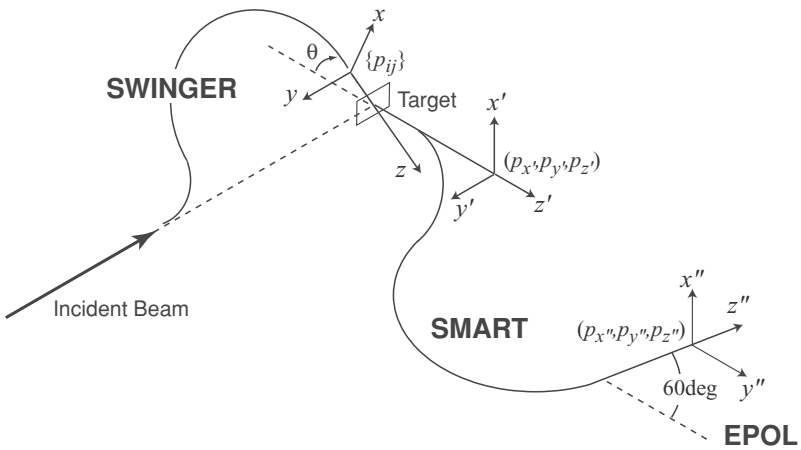

FIG. 6. Definition of the coordinate frame for the polarization observables at the SMART system. $\{p_{ij}\}$ denotes the vector or tensor deuteron beam polarizations, $p_{i'}$ is the polarization of the scattered protons at the target position, and $p_{i''}$ is the polarization of the scattered protons at the second focal plane FP2.

proton beams were not available at the RARF, the induced polarization $P^{y'}$ in the $^{12}\mathrm{C}(p,\vec{p})^{12}\mathrm{C}$ elastic scattering was used to determine A_y^C. $P^{y'}$ is equal to the analyzing power A_y for the time-reversed reaction $^{12}\mathrm{C}(\vec{p},p)^{12}\mathrm{C}$, which has been precisely measured at $E_p =$ 200 MeV by Meyer *et al.* at IUCF [53]. Thus, in the first step we produced polarized proton beams by $^{12}\mathrm{C}(p,\vec{p})^{12}\mathrm{C}$ elastic scattering at $\theta_{\mathrm{lab.}} = 17.1^\circ$ and 27.1°, using unpolarized proton beams of 200 MeV energy and a 284-mg/cm^2-thick graphite target. Then, we created 168-MeV proton beams by reducing the energy of the elastically scattered protons with a brass plate installed downstream of the graphite target. The expected values of the polarizations $P^{y'}$ were 0.981 and -0.381 at $\theta_{\mathrm{lab.}} = 17.1^\circ$ and 27.1°, respectively. After momentum analysis by the magnetic spectrograph, the polarization analyzer target was bombarded by polarized proton beams. Because the y'' axis was in the horizontal plane in the SMART system (see Fig. 6), the up-down asymmetry was measured by the EPOL to extract the effective analyzing power A_y^C given by

$$A_y^C = \frac{\int I_{\mathrm{o}}(\theta) A_y(\theta) \cos\phi \, d\Omega}{\int I_{\mathrm{o}}(\theta) d\Omega}. \tag{1}$$

The numbers of events in the upper side, N_U, and the lower side, N_D, regions were obtained as

$$N_U = \int_{-\Delta\phi}^{\Delta\phi} \int_{\theta_{\min}}^{\theta_{\max}} I_{\mathrm{o}}(\theta)[1 + A_y(\theta) p_{y''} \cos\phi] d\Omega, \tag{2}$$

$$N_D = \int_{-\Delta\phi+\pi}^{\Delta\phi+\pi} \int_{\theta_{\min}}^{\theta_{\max}} I_{\mathrm{o}}(\theta)[1 + A_y(\theta) p_{y''} \cos\phi] \, d\Omega. \tag{3}$$

Here, $I_{\mathrm{o}}(\theta)$ and $A_y(\theta)$ are the cross section and analyzing power for inclusive proton scattering in the carbon analyzer of the EPOL. $p_{y''}$ is the proton beam polarization at FP2. Angular integrations in Eqs. (2) and (3) were performed over regions of polar and azimuthal angles of $5^\circ \leqslant \theta \leqslant 20^\circ$ and $\Delta\phi = 60^\circ$, respectively.

The proton spin precessed around the vertical axis of the spectrograph. The spin precession angle χ with respect to the direction of the proton momentum is given in the moving frame by $\chi = \gamma(g/2 - 1)\Theta_D$, where γ is the Lorentz factor $\gamma = (m_p c^2 + E_p)/m_p c^2$, g is the spin g factor of the proton, and Θ_D is the bending angle of the spectrograph. The total bending angle of the magnetic spectrograph is $\Theta_D = 60^\circ$. This precession gives

$$p_{y''} = P^{y'} \cos\chi. \tag{4}$$

The energy-dependent curve of A_y^C was obtained by fitting the effective analyzing powers calculated from the empirical energy-dependent fit of the inclusive analyzing powers for the $p + \mathrm{C}$ reaction by McNaughton *et al.* [54] and the angular distributions of the differential cross section of Aprile-Giboni *et al.* [55]. The obtained curve was scaled to adjust the experimentally obtained A_y^C. The uncertainty of the input parameters for the $p + \mathrm{C}$ inclusive analyzing power [54] is 2%. The uncertainty of the fit for the energy-dependent curve is 5%. Thus, the estimated overall systematic uncertainty of the effective analyzing power A_y^C of EPOL is 6% at most.

3. Extraction of analyzing powers and polarization transfer coefficients

The deuteron analyzing powers and polarization transfer coefficients for the coplanar configurations of the breakup reaction $\vec{d} + p \to \vec{p}_1 + p_2 + n$ are expressed through the unpolarized (σ_0) and polarized (σ) cross sections together with the polarizations of the incoming deuteron (p_{ij}) and the proton $p_1(p_{k'})$ as

$$\sigma/\sigma_0 = 1 + \tfrac{3}{2} p_y A_y^d + \tfrac{2}{3} p_{xz} A_{xz} + \tfrac{1}{3}(p_{xx} A_{xx} + p_{yy} A_{yy} + p_{zz} A_{zz}), \tag{5}$$

$$p_{y'}\sigma/\sigma_0 = P^{y'} + \tfrac{3}{2} p_y K_y^{y'} + \tfrac{2}{3} p_{xz} K_{xz}^{y'} + \tfrac{1}{3}\left(p_{xx} K_{xx}^{y'} + p_{yy} K_{yy}^{y'} + p_{zz} K_{zz}^{y'}\right), \tag{6}$$

where x, y, and z and x', y', and z' are the sets of coordinates used to describe the polarization of the incident deuteron and the proton p_1, respectively [52]. We rotated the spin direction to the y axis for the A_y^d, A_{yy}, $K_y^{y'}$, and $K_{yy}^{y'}$ measurements, and to the x axis for the A_{xx} measurement. For the A_{xz} measurement, the spin symmetry axis was rotated into the reaction plane and inclined at an angle β to the beam direction.

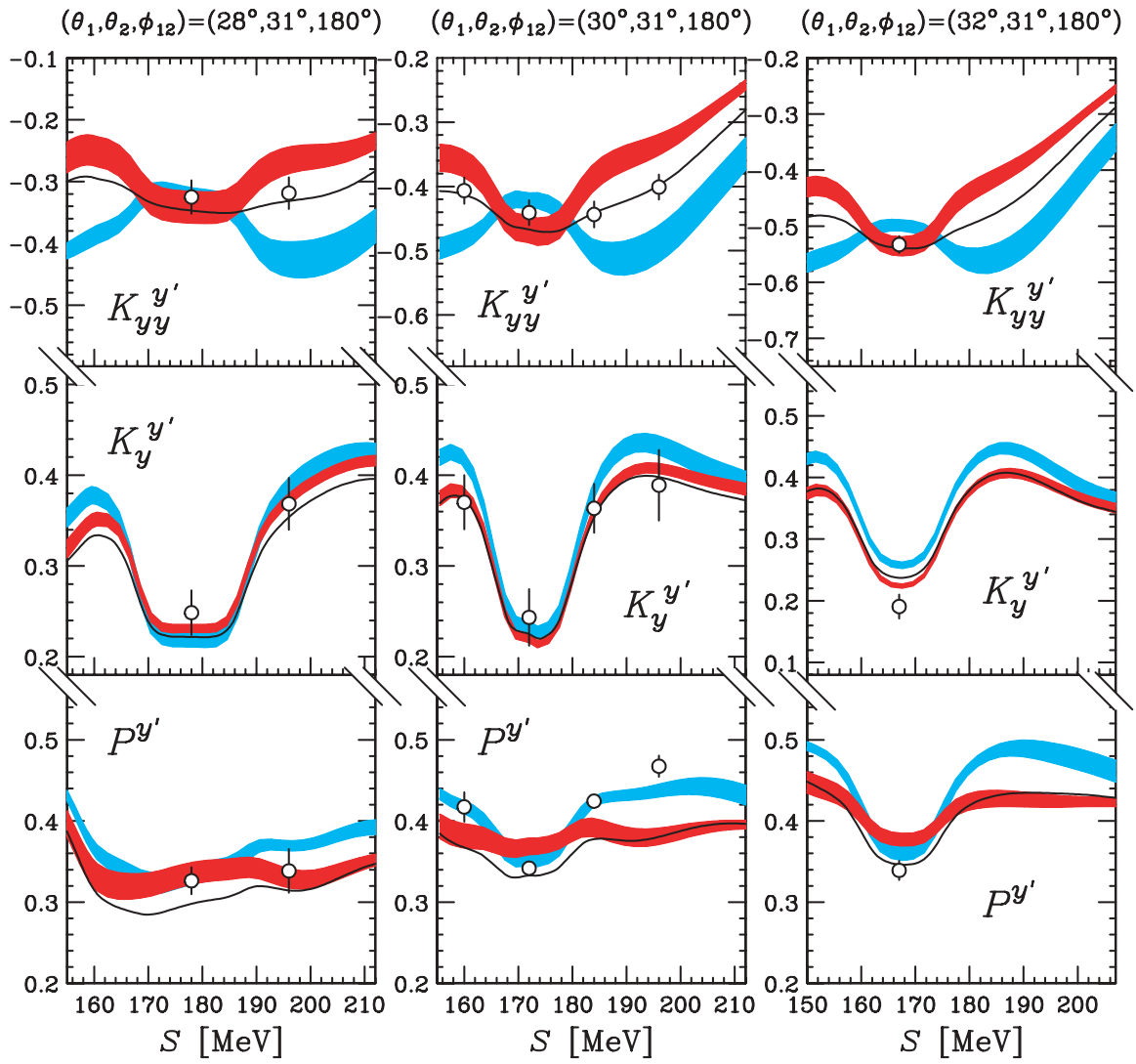

FIG. 7. (Color online) Polarization transfer coefficients $K_{yy}^{y'}$ and $K_{y}^{y'}$ and the induced polarization $P^{y'}$ for the kinematically complete breakup reaction ^{1}H($\vec{d}$, $\vec{p}_1 p_2$)n at 135 MeV/nucleon at the central positions of the detectors (θ_1, θ_2, ϕ_{12}, as labeled at the top of each column) in the laboratory system. The shown S values are obtained with the nonrelativistic frame, and the experimental S values obtained with the relativistic frame are shifted by δS for each kinematical configuration (see text). The light shaded bands indicate the NN force predictions obtained with the AV18, CD-Bonn, Nijmegen I, and Nijmegen II potentials, and the dark shaded bands indicate the predictions when they are combined with the TM′(99) 3NF as described in the text. The solid curve is the AV18 + Urbana IX 3NF prediction. All the theoretical predictions are point-geometry results averaged over the same energy bin ΔS as the data (see text).

Thus, the polarized cross sections were given as

$$p_{y'}\sigma/\sigma_0 = P^{y'} + \tfrac{3}{2} p_y K_y^{y'} + \tfrac{1}{2} p_{yy} K_{yy}^{y'} \text{ for } K_y^{y'} \text{ and } K_{yy}^{y'}, \quad (7)$$

$$\sigma/\sigma_0 = 1 + \tfrac{3}{2} p_y A_y^d + \tfrac{1}{2} p_{yy}\, A_{yy} \text{ for } A_y^d \text{ and } A_{yy}, \quad (8)$$

$$\sigma/\sigma_0 = 1 + \tfrac{1}{2} p_{xx}\, A_{xx} \text{ for } A_{xx}, \quad (9)$$

$$\sigma/\sigma_0 = 1 + \tfrac{2}{3} p_{xz}\, A_{xz} + \tfrac{1}{3}(p_{xx} - p_{zz})\, A_{xx} + \tfrac{1}{3}(p_{yy} - p_{zz})\, A_{yy} \text{ for } A_{xz}, \quad (10)$$

with

$$A_{xx} + A_{yy} + A_{zz} = 0.$$

$p_{y'}$ was obtained using Eqs. (1)–(4) as

$$p_{y'} = \frac{1}{A_y^C \cos\chi} \left(\frac{N_U - N_D}{N_U + N_D} \right). \quad (11)$$

The value of A_{xz} was extracted by using the measured A_{xx} and A_{yy} values.

The experimental results for the polarization transfer coefficients $K_{yy}^{y'}$ and $K_{y}^{y'}$, the induced polarization $P^{y'}$, and the analyzing powers A_y^d, A_{yy}, A_{xx}, and A_{xz} in the three configurations with the central angle sets $(\theta_1, \theta_2, \phi_{12}) = (28^\circ, 31^\circ, 180^\circ)$, $(30^\circ, 31^\circ, 180^\circ)$, and $(32^\circ, 31^\circ, 180^\circ)$ are shown with open circles along the kinematical S curve in Figs. 7 and 8. The statistical uncertainties are less than 0.03 for $K_{yy}^{y'}$ and $P^{y'}$, less than 0.04 for $K_{y}^{y'}$, less than 0.02 for

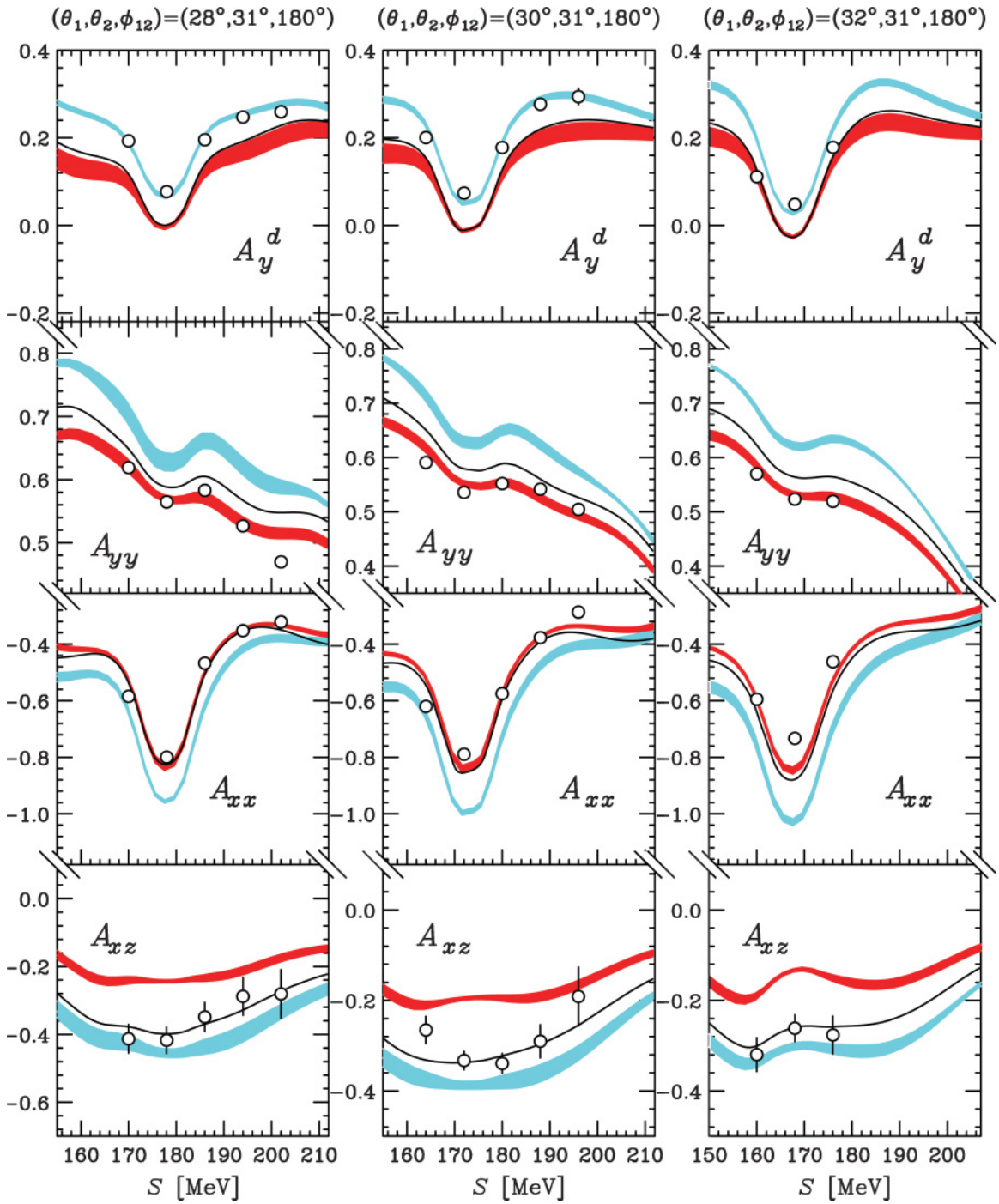

FIG. 8. (Color online) Deuteron analyzing powers A_y^d, A_{xx}, A_{yy}, and A_{xz} for the complete breakup reaction ^{1}H($\vec{d}$, p_1p_2)n at 135 MeV/nucleon and at the central positions of the detectors ($\theta_1, \theta_2, \phi_{12}$), as labeled. For the descriptions of bands and curves see Fig. 7. All the theoretical predictions are point-geometry results averaged over the same energy bin ΔS as the data (see text).

A_y, A_{yy}, and A_{xx}, and less than 0.07 for A_{xz}. As described in the previous sections, the data have been obtained with averaging over the finite angular range of the polar angle $\Delta\theta_1 = \pm 1°$ and the azimuthal angle $\Delta\phi_1 = \pm 1.4°$ for the proton p_1 and over the finite hole aperture $\Delta\theta_2 = 0.8°$ for the proton p_2. The relative central azimuthal angle between p_1 and p_2, defined as ϕ_{12}, was 180°. The data have been averaged over $\Delta S = 8$ MeV for A_y^d, A_{yy}, A_{xx}, and A_{xz}, over $\Delta S = 18$ MeV for $K_{yy}^{y'}$ at $\theta_1 = 28°$, and over $\Delta S = 12$ MeV for $K_{yy}^{y'}$ at $\theta_1 = 30°$ and 32°.

The uncertainties of the kinetic energies of the two scattered protons influence the position of the bin along the kinematical arc length S and cause the measured observables to be modified. The time-dependent fluctuations of the kinetic energy E_1, induced by time variation of the magnetic fields,

were monitored by measuring the magnetic fields of the spectrometer during the experiment. Their values were found to be less than 1%. Those of the E_2 detector were monitored by the peak positions of the scattered deuterons from the elastic dp scattering throughout the experiment, and found to be less than 2%. The modifications of the polarization observables due to the uncertainties of the kinetic energies E_1 and E_2 are estimated to be 0.01 or less.

Uncertainties of the scattering angles originate from the finite angular resolution, finite target thickness, and the size of the beam spot on the target. The angular resolution of the scattering angle θ_1 is determined by ion optical analysis of the SMART spectrograph and is estimated to be less than 0.2° [19]. The uncertainty of the setting angle θ_2 originates from the mechanical construction of the scattering chamber, and it is estimated to be less than 0.2°. The uncertainties from the finite target thickness and the size of the beam spot are estimated to be less than 0.3°. The modifications of observables caused by the uncertainties of the scattering angles are estimated by theoretical predictions averaged over the finite angles. Their values are far less than the statistical uncertainties.

The uncertainty of the deuteron beam polarizations is less than 3%. The variation of the polarization transfer coefficients originating from the uncertainty of the bending angle of the spectrometer is less than 1%. The uncertainty of the effective analyzing power for the EPOL is 6%. Thus the overall systematic uncertainties are estimated to be 7% at most for the polarization transfer coefficients and the induced polarization $P^{y'}$, and about 3% for all the deuteron analyzing powers.

IV. THEORETICAL FORMALISM AND DYNAMICAL INPUT

In this paper, we study the complete Nd breakup reaction with an initial state ϕ composed of a deuteron and a nucleon with specific spin projections and moving with relative momentum $\mathbf{q}_0$. The outgoing state ϕ_0 contains three free nucleons with specific momenta and spin projections. The transition matrix element for the breakup reaction $\langle\phi_0|U_0|\phi\rangle$ is given by an operator T which fulfills $3N$ Faddeev equations

$$\langle\phi_0|U_0|\phi\rangle = \langle\phi_0|(1+P)T|\phi\rangle. \tag{12}$$

From the matrix elements, various breakup spin observables and cross sections can be calculated [52,56].

The $3N$ Faddeev equation for the T operator sums up all the rescatterings induced by the two- and three-nucleon forces acting between nucleons into the integral equation [56,57]

$$\begin{aligned} T &= tP\phi + (1+tG_0)V_4^{(1)}(1+P)\phi \\ &\quad + tPG_0T + (1+tG_0)V_4^{(1)}(1+P)G_0T. \end{aligned} \tag{13}$$

The quantity G_0 is the free $3N$ propagator and P takes into account the identity of nucleons and is the sum of a cyclical and an anticyclical permutation of three nucleons. $V_4^{(1)}$ represents one of the terms of the $3N$ force V_4

$$V_4 = V_4^{(1)} + V_4^{(2)} + V_4^{(3)}, \tag{14}$$

where each $V_4^{(i)}$ is symmetric under the exchange of nucleons jk with $j \neq i \neq k$. In the 2π-exchange 3NF, $V_4^{(1)}$ contributes to the $3N$ potential from (off-shell) rescattering of a pion on nucleon 1. The NN off-shell t matrix results from a given NN potential through the Lippmann-Schwinger equation.

After projecting on a partial-wave momentum-space basis, this equation leads to a system of coupled integral equations which can be solved numerically exactly for any nuclear force. In this study, we restrict our partial-wave basis so that it includes only states with total angular momenta j in the two-nucleon subsystem of less than six. This corresponds to a maximum of 142 partial-wave states in the $3N$ system for each total angular momentum. For the energies of the present paper, this provides convergent results for the breakup observables. We compared the convergence against the results obtained when $j = 6$ states were included. This increased the number of states to 194. This convergence check was done without the 3NF. The inclusion of the 3NF was carried out for all total angular momenta of the $3N$ system up to $J = 13/2$, while the longer ranged $2N$ interactions require states up to $J = 25/2$. For details of the formalism and the numerical performance, see Refs. [56–59].

In this study, we show the predictions of different nuclear force models. They consist of realistic NN potentials: AV18 [1], CD-Bonn [3], Nijmegen I, and Nijmegen II [4], and two 3NF models: Tucson-Melbourne (TM) [7] and Urbana IX [8]. The standard parametrization of the TM 3NF was criticized in Refs. [34,35,60] since it violates chiral symmetry. A form more consistent with chiral symmetry was proposed by modifying the c term of the TM force and incorporating the long-range part of this term into the a term and rejecting the rest of the c term [34,35]. This new form is called TM′99 [33]. Each NN interaction was combined with the TM′99 3NF model, and the cutoff parameter Λ in the strong form factor parametrization was separately adjusted to the ^{3}H binding energy [61]. The Λ values for the AV18, CD-Bonn, Nijmegen I, and Nijmegen II potentials were found to be $\Lambda = 4.764, 4.469, 4.690,$ and 4.704 (in units of m_π), respectively.

For the AV18 potential we used in addition the Urbana IX 3NF [8]. This force is based on an intermediate Δ excitation in the 2π exchange [6], which is augmented by a phenomenological spin-independent short-range part. Originally, Urbana IX was formulated in configuration space [8]. We refer to Ref. [62] for the partial-wave decomposition of the Urbana IX 3NF in momentum space.

To estimate the relativistic effects on the studied breakup spin observables, we solved Eq. (13) with pairwise forces only, including relativistic kinematics, boost effects, and Wigner rotation of spin states. We followed the approach presented in Refs. [63,64]. For the convenience of the reader, we briefly describe that approach in the following.

The formal structures of the nonrelativistic and relativistic Faddeev equations are the same, and only the components should be modified. The relativistic kinetic energy H_0 of three equal mass (m) nucleons in their $3N$ c.m. system can be written as [63]

$$H_0 = \sqrt{(2\omega(\mathbf{k}))^2 + \mathbf{q}^2} + \sqrt{m^2 + \mathbf{q}^2}, \tag{15}$$

where $2\omega(\mathbf{k}) \equiv 2\sqrt{m^2 + \mathbf{k}^2}$ and $\mathbf{q}$ is the momentum of the third nucleon, whereas $-\mathbf{q}$ is the total momentum of the chosen two-body subsystem. In that two-body subsystem, the two nucleons have momenta $\mathbf{k}$ and $-\mathbf{k}$, respectively. Theyf are connected to the individual nucleon momenta in an arbitrary frame by a free Lorentz transformation.

The full $3N$ Hamiltonian besides H_0 contains the sum of the pair interactions $V(\mathbf{q})$ between the nucleons, of the form

$$V(\mathbf{q}) \equiv \sqrt{(2\omega(\mathbf{k}) + v)^2 + \mathbf{q}^2} - \sqrt{(2\omega(\mathbf{k}))^2 + \mathbf{q}^2}, \quad (16)$$

where v is the relativistic potential defined in the $2N$ c.m. system.

Equations (15) and (16) define new components that enter Eq. (13): the boosted t operator, which satisfies the relativistic $2N$ Lippmann-Schwinger equation

$$t(\mathbf{k}, \mathbf{k}'; \mathbf{q}) = V(\mathbf{k}, \mathbf{k}'; \mathbf{q}) + \int d^3k'' \times \frac{V(\mathbf{k}, \mathbf{k}''; \mathbf{q})\, t(\mathbf{k}'', \mathbf{k}'; \mathbf{q})}{\sqrt{(2\omega(\mathbf{k}'))^2 + \mathbf{q}^2} - \sqrt{(2\omega(\mathbf{k}''))^2 + \mathbf{q}^2} + i\epsilon}, \quad (17)$$

and the relativistic $3N$ propagator

$$G_0 = \frac{1}{E + i\epsilon - H_0}, \quad (18)$$

where E is the total $3N$ c.m. energy.

For the technical performance, the momentum space partial-wave decomposition, and the corresponding expression of the permutation operator P matrix elements, we refer to Refs. [63,64], which also detail the solution to the relativistic Faddeev equations.

As dynamical input for our relativistic calculations, we used the relativistic interaction $V(\mathbf{q})$ generated from the nonrelativistic NN potential CD-Bonn according to the iterative procedure of Ref. [65]. This relativistic NN interaction is exactly on-shell equivalent to the underlying nonrelativistic potential. In our relativistic calculations, we also included Wigner spin rotations as described in detail in Ref. [64]. To check the size of the effects on our spin observables, we also performed relativistic calculations neglecting Wigner rotations completely. As for nonrelativistic calculations, all the relativistic calculations took into account all the partial-wave states with total angular momenta j in the two-nucleon subsystem less than six.

V. RESULTS AND DISCUSSION

A. Modifications of the point-geometry theory

In this study, we compare experimental data with theoretical predictions based on Faddeev calculations with different NN potentials either combined with or without various 3NFs. For this, the point-geometry theoretical predictions should be averaged over the finite angular resolutions of the proton detectors and also integrated over the energy bin ΔS of the kinematical S curve used in the data analysis. To estimate the resulting effect, we integrated the point-geometry predictions over the angular aperture of both detectors. For each pair of angles contributing to the integral, the cross section along the corresponding S curve was projected on the central S curve defined by the central positions of both detectors. In addition, averaging over the energy bin ΔS was performed with ΔS taken to be the same as for the data averaging. In Fig. 9, an example for the resulting modifications of the point-geometry theory based on the AV18 potential combined with the Urbana IX 3NF is shown for the vector analyzing power A_y^d at $(\theta_1, \theta_2, \phi_{12}) = (28^\circ, 31^\circ, 180^\circ)$. The solid curve is the point-geometry prediction, while the changes to the point-geometry predictions by the finite angular resolutions alone are shown by the dot-dot-dashed curve. The effects of averaging over ΔS alone are shown by the dashed curve. The dotted curve is obtained for the finite geometry with additional averaging over the energy bin ΔS. We found that the modifications due to the finite angular resolutions of the detectors are small for all three configurations and for all observables in the present measurement. The largest change is due to averaging over the energy bin ΔS. Therefore, in the following, we compare the data with the point-geometry theoretical predictions averaged over the same energy bin ΔS as used for the data averaging.

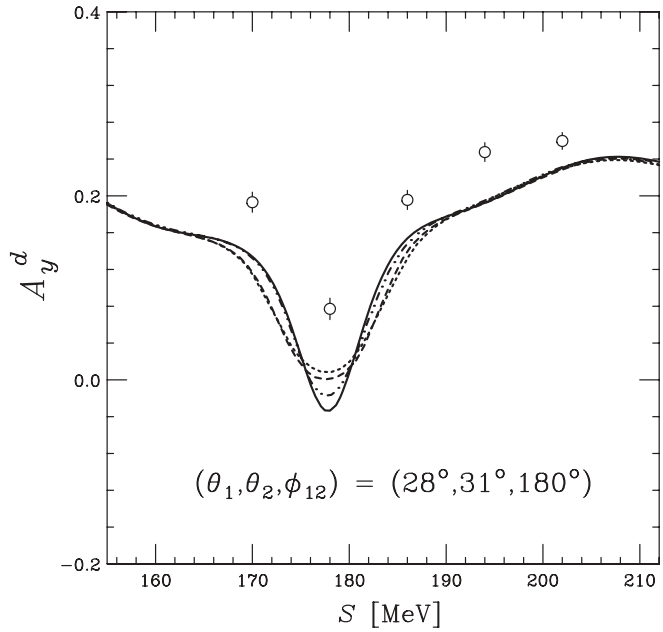

FIG. 9. Theoretical prediction for A_y^d in the configuration at $(\theta_1, \theta_2, \phi_{12}) = (28^\circ, 31^\circ, 180^\circ)$ based on the AV18 potential combined with the Urbana IX 3NF. The solid curve is a point-geometry prediction and the dot-dot-dashed curve is a finite-geometry prediction. The dashed and dotted curves are obtained with point and finite geometries, respectively, and averaged over the energy bin $\Delta S =$ 8 MeV.

The kinematical S curve used in the data analysis was calculated with relativistic kinematics, while the S curve for the theoretical predictions is nonrelativistic. Those two curves are different at the energy considered for all three configurations. Figure 10 demonstrates this for the configuration at $(\theta_1, \theta_2, \phi_{12}) = (30^\circ, 31^\circ, 180^\circ)$. The solid curve is a relativistic S curve, and the dotted curve is a nonrelativistic curve. Starting

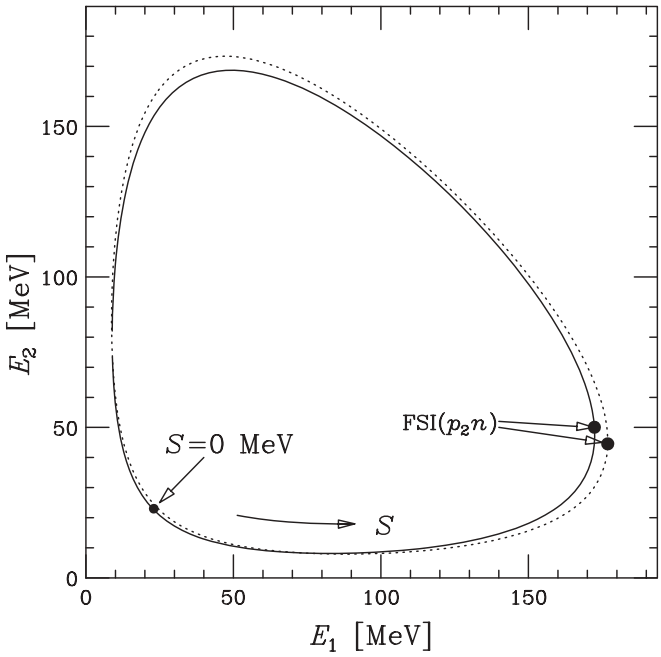

FIG. 10. Kinematical S curve for the configuration at $(\theta_1, \theta_2, \phi_{12}) = (30^\circ, 31^\circ, 180^\circ)$. The solid curve is the S curve calculated with relativistic kinematics, while the dotted curve is the S curve calculated with nonrelativistic kinematics.

with $S = 0$ as shown in Fig. 10 (see also Sec. III A), the difference $\delta S \equiv S(\text{nonrelativistic}) - S(\text{relativistic})$ becomes 7.5 MeV at the point on the S curve where FSI(p_2n) occurs. To see how the nonrelativistic theoretical predictions explain the measured observables, we shifted the S value of the analyzed data by δS, setting the experimental S value at the FSI(p_2n) to the nonrelativistic FSI(p_2n) S value. This procedure was applied also to the other two configurations. The δS values at $(\theta_1, \theta_2, \phi_{12}) = (28^\circ, 31^\circ, 180^\circ)$ and $(32^\circ, 31^\circ, 180^\circ)$ are 7 and 8 MeV, respectively.

B. Comparison of the data with theoretical predictions

In Figs. 7 and 8 we compare measured polarization transfer coefficients and deuteron analyzing powers with the point-geometry theoretical predictions for the four different NN potentials alone (light shaded bands) or combined with the TM′99 3NF (dark shaded bands). The solid curves are the theoretical predictions obtained using the AV18 potential combined with the Urbana IX 3NF. The nonrelativistic S values are expressed in the figures and the experimental S values are shifted by δS for each configuration (see Sec. V A).

The deuteron to proton polarization transfer coefficient $K_{yy}^{y'}$ exhibits strong dependence on the nuclear forces (see top panels in Fig. 7). The pure NN force prediction has for all three kinematical configurations a maximum in the region of S values around the p_2n FSI point. Including a 3NF, either the TM′99 or the Urbana IX, drastically changes the shape of the predictions. Instead of a maximum around the p_2n FSI point, a minimum is created when a 3NF is added. The TM′99 and Urbana IX provide similar values for $K_{yy}^{y'}$ around the p_2n FSI. However, the predicted values are drastically different and depend on the 3NF models in S regions away from the p_2n FSI. Our data clearly deviate from the NN force predictions in all three kinematical configurations. For the two at $(\theta_1, \theta_2, \phi_{12}) = (28^\circ, 31^\circ, 180^\circ)$ and $(30^\circ, 31^\circ, 180^\circ)$, the Urbana IX 3NF predictions provide a much better description of the data than the TM′99 3NF.

For the deuteron to proton polarization transfer coefficient $K_y^{y'}$, the 3NF effects are not as strongly pronounced as for $K_{yy}^{y'}$ (see Fig. 7). Including the TM′99 or Urbana IX 3NF leads to modifications to the NN force theory, and both 3NFs provide similar values for $K_y^{y'}$. In all three configurations, the data seem to support the theoretical predictions with a 3NF included, especially for the two configurations at $(\theta_1, \theta_2, \phi_{12}) = (28^\circ, 31^\circ, 180^\circ)$ and $(30^\circ, 31^\circ, 180^\circ)$.

The induced polarization $P^{y'}$ of the outgoing proton p_1 again shows large 3NF effects in some regions of the S curve (see Fig. 7). Similar to the polarization transfer coefficient $K_{yy}^{y'}$, there are strong differences between the effects of the TM′99 and Urbana IX 3NFs, localized in some regions of the S curve. In contrast to $K_{yy}^{y'}$ and $K_y^{y'}$, the data for the configuration at $(30^\circ, 31^\circ, 180^\circ)$ seem to support the theoretical predictions obtained without 3NFs for the induced polarization.

Large 3NF effects are also seen for the tensor analyzing powers (see Fig. 8). For A_{xz}, the TM′99 and Urbana IX 3NFs provide very different results. The effects of the TM′99 3NF are about a factor of 3 larger than the effects of Urbana IX. The A_{xz} data nicely agree with the AV18 + Urbana IX predictions for all measured configurations. Large 3NF effects are also seen for the tensor analyzing powers A_{xx} and A_{yy}. For A_{xx}, they depend only slightly on the 3NF model and the data nicely agree with the NN + 3NF predictions. The tensor analyzing power A_{yy} is more sensitive to the 3NF model and the data are well described by the NN + TM′99 combination.

The results for the vector analyzing power A_y^d contrast with those for the tensor analyzing powers (see Fig. 8). The pure NN force predictions provide quite a good description of the data. Including the TM′99 or Urbana IX 3NF causes large and model-independent effects; however, description of the data is poorer than that for NN forces alone. It is interesting to note that our results for the breakup analyzing powers are different from those found for these observables in elastic dp scattering. In this case, the vector analyzing power A_y^d data can be explained by the theoretical predictions including the 3NF, while the tensor analyzing powers A_{xx}, A_{yy}, and A_{xz} cannot be explained by any of the theoretical predictions [19,32].

At the energy of the present study, the S curve calculated with nonrelativistic kinematics already differs from the corresponding relativistic S curve for our three geometries, especially around the final state interaction point FSI (p_2n) (see Fig. 10 and Sec. V A). To show how large the effects on our spin observables due to relativity are, we present in Figs. 11 and 12 the theoretical predictions based on the CD-Bonn potential alone in the nonrelativistic case (dotted curves) and those in the relativistic case including relativistic kinematics, boost effects, and Wigner spin rotations (solid curves). Relativistic predictions obtained without Wigner spin

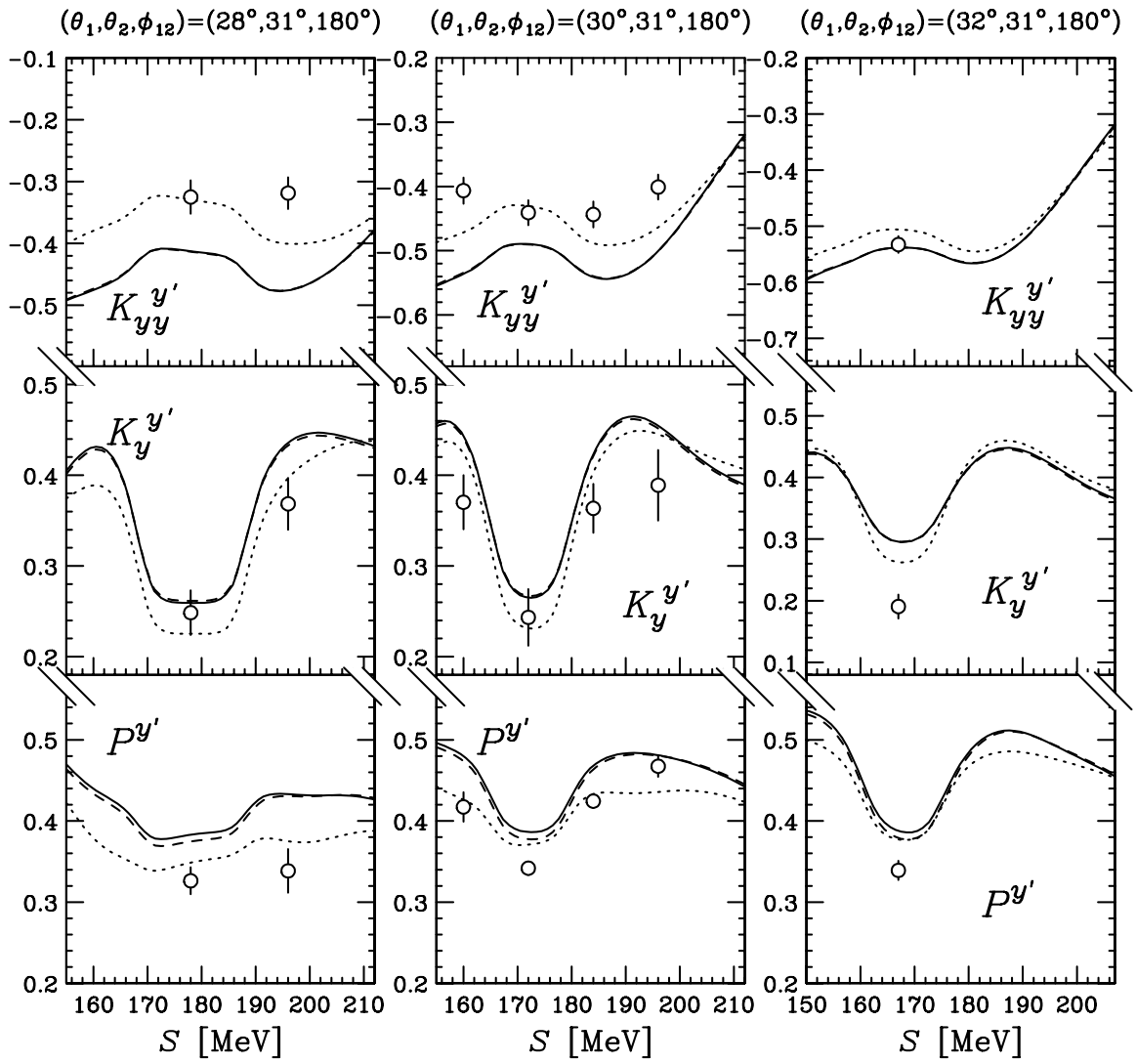

FIG. 11. Polarization transfer coefficients $K_{yy}^{y'}$ and $K_{y}^{y'}$, and the induced polarization $P^{y'}$ for the complete breakup reaction ^{1}H$(\vec{d}, \vec{p}_1 p_2)n$ at 135 MeV/nucleon and at the central positions of the detectors $(\theta_1, \theta_2, \phi_{12})$ as labeled. The dotted curve is the CD-Bonn nonrelativistic prediction. The solid and dashed curves are relativistic predictions based on the CD-Bonn potential with and without Wigner spin rotations, respectively. The S values of the relativistic predictions (solid and dashed curves) are shifted by δS (see Sec. V A). All the theoretical predictions are point-geometry results averaged over the same energy bin ΔS as the experimental data (see text).

rotations are also shown (dashed curves). The results shown in Figs. 11 and 12 are point-geometry predictions averaged over the same energy bin ΔS as used for the data averaging. Note that to demonstrate the magnitude of the relativistic effects, the S values of the relativistic predictions (solid and dashed curves) are shifted by δS, as for Figs. 7 and 8 (see Sec. V A).

It can be seen that the relativistic effects modify the values predicted nonrelativistically for our breakup spin observables and are not negligible in the region around FSI $(p_2 n)$. Their magnitude depends on the observable, the central positions of the proton detectors, and the position on the S curve. The relativistic effects are largest for the tensor analyzing power A_{xz} (changes up to ≈25%), the polarization transfer coefficients $K_{yy}^{y'}$ (changes up to ≈30%) and $K_{y}^{y'}$ (changes up to ≈17%), and the induced polarization $P^{y'}$ (changes up to ≈16%). A relativistic treatment increases the absolute magnitude of the polarization transfer coefficients and induced polarizations, whereas it decreases A_{xz}. Despite these effects, assuming that the relativistic and 3NF effects act incoherently, accounting for relativity does not change the conclusions based on the nonrelativistic calculations for the importance of the 3NF for explaining the data for polarization transfer coefficients and induced polarizations, except for $K_{yy}^{y'}$.

For the analyzing powers A_y^d, A_{xx}, and A_{yy} close to FSI $(p_2 n)$, the relativistic effects are practically negligible. For all analyzing powers including A_{xz}, the incoherent impact of the relativistic and 3NF effects leads to a similar description of our data as for the nonrelativistic 3NF calculations.

For all the studied breakup spin observables in all geometries, the effects of Wigner spin rotations are negligible (see Figs. 11 and 12).

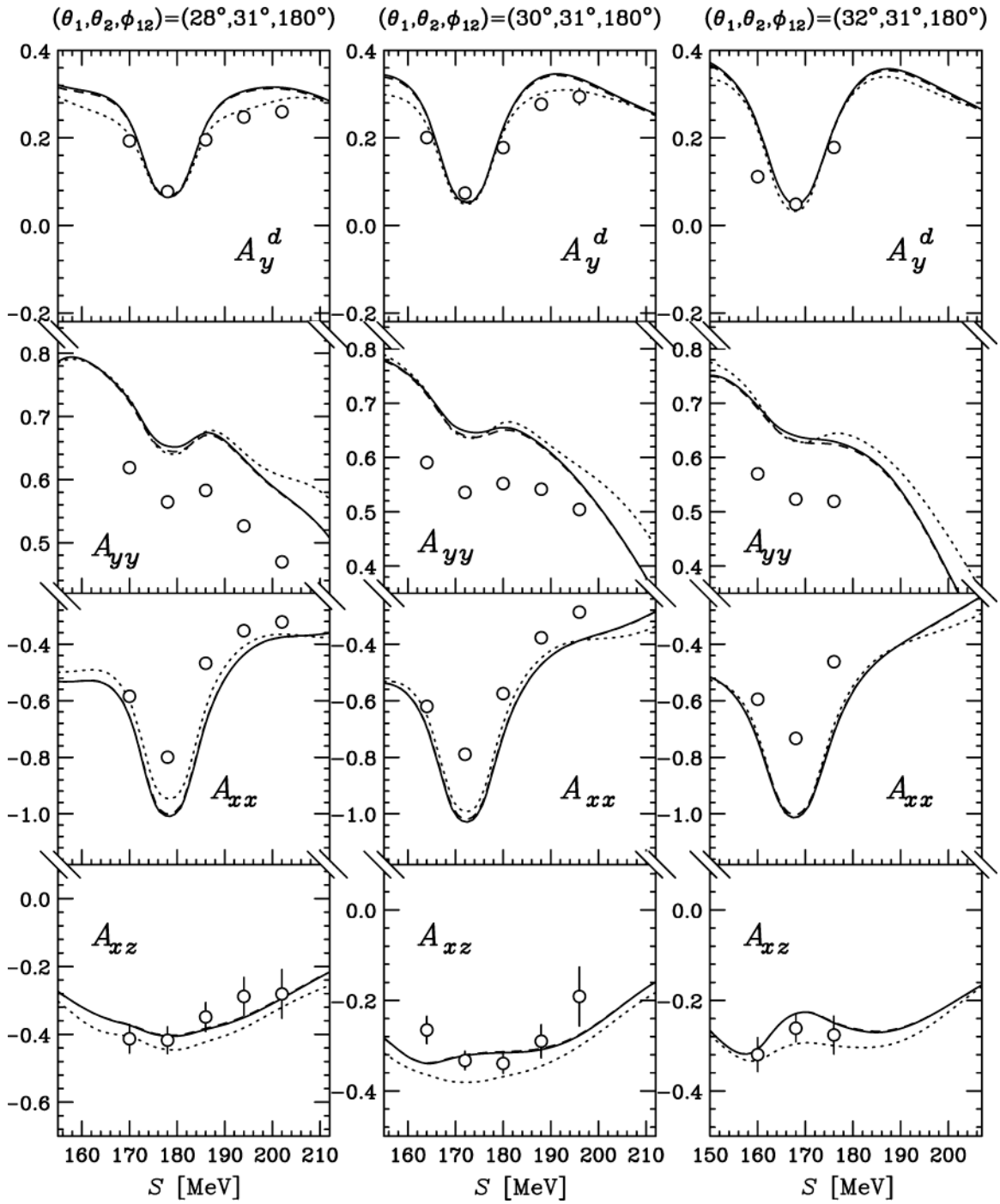

FIG. 12. Deuteron analyzing powers A_y^d, A_{xx}, A_{yy}, and A_{xz} for the complete breakup reaction ^{1}H($\vec{d}$, p_1p_2)n at 135 MeV/nucleon and at the central positions of the detectors (θ_1, θ_2, ϕ_{12}) as labeled. For the descriptions of the curves, see Fig. 11. All the theoretical predictions are point-geometry results averaged over the same energy bin ΔS as the data (see text).

VI. SUMMARY AND CONCLUSIONS

The experiment on the kinematically complete dp breakup reaction $d + p \rightarrow p_1 + p_2 + n$ was performed with polarized deuteron beams of 135-MeV/nucleon energy. To discriminate between the two 2π-exchange 3NF models—TM′99 and the Urbana IX—we focused on the measurement of the deuteron to proton polarization transfer coefficient $K_{yy}^{y'}$ in three coplanar configurations, which give different theoretical predictions for $K_{yy}^{y'}$ under these models. The measured kinematical configurations correspond to the angle of the emerging proton $p_1(\theta_1 = 28^\circ, 30^\circ,$ and $32^\circ)$ and to the angle of the second outgoing proton $p_2(\theta_2 = 31^\circ)$. The configurations include the final state interaction geometry between the proton p_2 and the undetected neutron, FSI(p_2n). In our measurement, the deuteron to proton polarization transfer coefficient $K_y^{y'}$ and the induced polarization $P^{y'}$ of the outgoing proton p_1 were

also simultaneously obtained. In addition, we measured all the deuteron analyzing powers A_y^d, A_{yy}, A_{xx}, and A_{xz}, for which large 3NF effects have been predicted. The statistical uncertainties of our data are smaller than 0.03 for $K_{yy}^{y'}$ and $P^{y'}$, and less than 0.04 for $K_y^{y'}$. For the deuteron analyzing powers, the statistical uncertainties are smaller than 0.02 for A_y^d, A_{yy}, and A_{xx}, and less than 0.07 for A_{xz}. The overall systematic uncertainties are estimated to be 7% at most for the polarization transfer coefficients and the induced polarization $P^{y'}$, and they are about 3% for all the deuteron analyzing powers.

We compared our data with the predictions based on different modern NN potentials, both combined and not combined with two 3NF models, the TM′99 and the Urbana IX. The Urbana IX 3NF is found to be superior in describing the polarization transfer coefficient $K_{yy}^{y'}$ and the tensor analyzing power A_{xz} in the three measured kinematical configurations. For the tensor analyzing power A_{xx}, both 3NF models give satisfactory descriptions of the data. For A_{yy}, a better description is provided by the TM′99 3NF. In contrast to the tensor analyzing powers, the vector analyzing power A_y^d data are described properly by the pure NN force predictions, while including 3NFs leads to a deterioration of this agreement. It was found that this behavior is opposite to that found in elastic dp scattering.

The nonrelativistic predictions based on the CD-Bonn potential were compared with the results of relativistic Faddeev calculations in which relativistic kinematics, boost effects, and Wigner spin rotations were incorporated. Large relativistic effects were found in the region of FSI (p_2n) for the tensor analyzing power A_{xz}, polarization transfer coefficients $K_{yy}^{y'}$ and $K_y^{y'}$, and the induced polarization $P^{y'}$. In all cases, the effects due to Wigner spin rotations were found to be negligible. Assuming incoherent summation of the relativistic and 3NF effects, the conclusions on the importance of 3NFs in explaining our data, found with nonrelativistic results, are not altered. However, further $3N$ Faddeev calculations should be performed to incorporate relativity and 3NFs at the same time.

In this work we have not considered effects due to the Coulomb interaction between the protons. In Ref. [66], large Coulomb interaction effects were found for the ^{1}H(d, pp)n breakup reactions at 65 MeV/nucleon in certain kinematical configurations. Especially significant effects of the Coulomb interaction were found for small relative azimuthal angles between the two outgoing protons at their small polar angles. Here, in contrast, we have focused on configurations around FSI(p_2n). These are not close to the ones where Coulomb effects have been seen in Ref. [66], but are very similar to the kinematical condition of dp elastic scattering at center-of-mass angles $\theta_{\text{c.m.}} = 110^\circ$–$120^\circ$, which corresponds to the minimum region of the elastic cross section. Therefore the effects of the Coulomb interactions are expected to be small for the measured data.

While the presented results clearly demonstrate the significance of our data in formulating a description of the structure of 3NFs, the measured spin observables in our coplanar configurations of the dp breakup reaction are not always explained by the current 3NFs, similar to the dp elastic scattering case. These results indicate that it is likely that some significant components of the 3NF other than the 2π-exchange contributions are missing in our calculations. Example candidate contributions in the traditional meson-exchange picture are π-ρ and ρ-ρ exchanges. This has to be expected since in χPT [15], in the order in which first-time nonvanishing 3NFs appear, there are three topologies of forces: the 2π-exchange, a one-pion exchange between one nucleon and a two-nucleon contact interaction, and a pure $3N$ contact interaction. They are of the same order and should be taken into account together. The latter two topologies could be modeled by π-ρ and ρ-ρ exchanges going back to the traditional meson-exchange picture. Therefore it would be reasonable to add the traditional meson-exchange picture as a further $3N$ force. It would be interesting to see how well our data are described by extended theoretical approaches, e.g., including 3NFs other than 2π-exchange types, a consistent relativistic treatment with 3NFs included, and potentials based on chiral effective field theory [15].

ACKNOWLEDGMENTS

We acknowledge the outstanding work of the RIKEN Accelerator group in delivering excellent polarized deuteron beams. We thank K. Sagara, T. Kudoh, H. Ohira, M. Tomiyama, and T. Ishida for their support during the test experiment of the detector at the Tandem Accelerator of Kyushu University. This work was supported financially in part by the Grants-in-Aid for Scientific Research Nos. 04402004 and 10304018 of the Ministry of Education, Culture, Sports, Science, and Technology of Japan. It was also partially supported by the Helmholtz Association through funds provided to the virtual institute "Spin and Strong QCD" (VH-VI-231), and by the 2008–2011 Polish Science Funds as a research project No. N N202 077435. The numerical calculations were performed on the IBM Regatta p690+ of the NIC in Jülich, Germany.

[1] R. B. Wiringa, V. G. J. Stoks, and R. Schiavilla, Phys. Rev. C **51**, 38 (1995).
[2] R. Machleidt, F. Sammarruca, and Y. Song, Phys. Rev. C **53**, R1483 (1996).
[3] R. Machleidt, Phys. Rev. C **63**, 024001 (2001).
[4] V. G. J. Stoks, R. A. M. Klomp, C. P. F. Terheggen, and J. J. de Swart, Phys. Rev. C **49**, 2950 (1994).
[5] A. Nogga, H. Kamada, and W. Glöckle, Phys. Rev. Lett. **85**, 944 (2000); A. Nogga, H. Kamada, W. Glöckle, and B. R. Barrett, Phys. Rev. C **65**, 054003 (2002).
[6] J. Fujita and H. Miyazawa, Prog. Theor. Phys. **17**, 360 (1957).
[7] S. A. Coon, M. D. Schadron, P. C. McNamee, B. R. Barrett, D. W. E. Blatt, and B. H. J. McKellar, Nucl. Phys. **A317**, 242 (1979); S. A. Coon and W. Glöckle, Phys. Rev. C **23**, 1790 (1981); S. A. Coon, Few-Body Syst. Suppl. **1**, 41 (1984); S. A. Coon and J. L. Friar, Phys. Rev. C **34**, 1060 (1986).

[8] B. S. Pudliner, V. R. Pandharipande, J. Carlson, S. C. Pieper, and R. B. Wiringa, Phys. Rev. C **56**, 1720 (1997).
[9] J. Carlson and R. Schiavilla, Rev. Mod. Phys. **70**, 743 (1998).
[10] R. B. Wiringa, S. C. Pieper, J. Carlson, and V. R. Pandharipande, Phys. Rev. C **62**, 014001 (2000); S. C. Pieper, K. Varga, and R. B. Wiringa, Phys. Rev. C **66**, 044310 (2002).
[11] S. C. Pieper and R. B. Wiringa, Annu. Rev. Nucl. Part. Sci. **51**, 53 (2001).
[12] S. C. Pieper, V. R. Pandharipande, R. B. Wiringa, and J. Carlson, Phys. Rev. C **64**, 014001 (2001).
[13] U. van Kolck, Phys. Rev. C **49**, 2932 (1994).
[14] E. Epelbaum, W. Glöckle, and U.-G. Meißner, Nucl. Phys. **A747**, 362 (2005).
[15] E. Epelbaum, Prog. Part. Nucl. Phys. **57**, 654 (2006).
[16] H. Witała, W. Glöckle, D. Hüber, J. Golak, and H. Kamada, Phys. Rev. Lett. **81**, 1183 (1998).
[17] N. Sakamoto *et al.*, Phys. Lett. **B367**, 60 (1996).
[18] H. Sakai *et al.*, Phys. Rev. Lett. **84**, 5288 (2000).
[19] K. Sekiguchi *et al.*, Phys. Rev. C **65**, 034003 (2002).
[20] K. Hatanaka *et al.*, Phys. Rev. C **66**, 044002 (2002).
[21] K. Sekiguchi *et al.*, Phys. Rev. Lett. **95**, 162301 (2005).
[22] K. Ermisch *et al.*, Phys. Rev. C **71**, 064004 (2005).
[23] P. Mermod *et al.*, Phys. Rev. C **72**, 061002(R) (2005).
[24] Y. Maeda *et al.*, Phys. Rev. C **76**, 014004 (2007).
[25] E. J. Stephenson, H. Witała, W. Glöckle, H. Kamada, and A. Nogga, Phys. Rev. C **60**, 061001(R) (1999).
[26] R. Bieber *et al.*, Phys. Rev. Lett. **84**, 606 (2000).
[27] K. Ermisch *et al.*, Phys. Rev. C **68**, 051001(R) (2003).
[28] H. R. Amir-Ahmadi *et al.*, Phys. Rev. C **75**, 041001(R) (2007).
[29] H. Mardanpour *et al.*, Eur. Phys. J. A **31**, 383 (2007).
[30] R. V. Cadman *et al.*, Phys. Rev. Lett. **86**, 967 (2001).
[31] B. v. Przewoski *et al.*, Phys. Rev. C **74**, 064003 (2006).
[32] K. Sekiguchi *et al.*, Phys. Rev. C **70**, 014001 (2004).
[33] S. A. Coon and H. K. Han, Few-Body Syst. **30**, 131 (2001).
[34] J. L. Friar, D. Hüber, and U. van Kolck, Phys. Rev. C **59**, 53 (1999).
[35] D. Hüber, J. L. Friar, A. Nogga, H. Witała, and U. van Kolck, Few-Body Syst. **30**, 95 (2001).
[36] A. Deltuva, A. C. Fonseca, and P. U. Sauer, Phys. Rev. C **71**, 054005 (2005).
[37] J. Kuroś-Żołnierczuk, H. Witała, J. Golak, H. Kamada, A. Nogga, R. Skibiński, and W. Glöckle, Phys. Rev. C **66**, 024003 (2002).
[38] St. Kistryn *et al.*, Phys. Rev. C **68**, 054004 (2003).
[39] St. Kistryn *et al.*, Phys. Rev. C **72**, 044006 (2005).
[40] H. O. Meyer *et al.*, Phys. Rev. Lett. **93**, 112502 (2004).
[41] M. Allet *et al.*, Phys. Rev. C **50**, 602 (1994).
[42] M. Allet *et al.*, Few-Body Syst. **20**, 27 (1996).
[43] J. Zejma *et al.*, Phys. Rev. C **55**, 42 (1997).
[44] K. Bodek *et al.*, Few-Body Syst. **30**, 65 (2001).
[45] T. Ichihara *et al.*, Nucl. Phys. **A569**, 287c (1994).
[46] H. Sakai *et al.*, Phys. Rev. Lett. **97**, 150405 (2006).
[47] H. Okamura *et al.*, AIP Conf. Proc. **293**, 84 (1994).
[48] H. Okamura *et al.*, AIP Conf. Proc. **343**, 123 (1995).
[49] K. Suda *et al.*, Nucl. Instrum. Methods Phys. Res. A **572**, 745 (2007).
[50] T. Uesaka *et al.*, RIKEN Accel. Prog. Rep. **35**, 148 (2002).
[51] H. Okamura, Nucl. Instrum. Methods Phys. Res. A **443**, 194 (2000).
[52] G. G. Ohlsen, Rep. Prog. Phys. **35**, 717 (1972).
[53] H. O. Meyer, P. Schwandt, G. L. Moake, and P. P. Singh, Phys. Rev. C **23**, 616 (1981).
[54] M. W. McNaughton *et al.*, Nucl. Instrum. Methods Phys. Res. A **241**, 435 (1985).
[55] E. Aprile-Giboni, R. Hausammann, E. Heer, R. Hess, C. Lechanoine-Le Luc, W. Leo, S. Morenzoni, Y. Onel, and D. Rapin, Nucl. Instrum. Methods Phys. Res. **215**, 147 (1983).
[56] W. Glöckle, H. Witała, D. Hüber, H. Kamada, and J. Golak, Phys. Rep. **274**, 107 (1996).
[57] D. Hüber, H. Kamada, H. Witała, and W. Glöckle, Acta Phys. Pol. B **28**, 1677 (1997).
[58] H. Witała, Th. Cornelius, and W. Glöckle, Few-Body Syst. **3**, 123 (1988).
[59] D. Hüber, H. Witała, and W. Glöckle, Few-Body Syst. **14**, 171 (1993).
[60] S. N. Yang, Phys. Rev. C **10**, 2067 (1974).
[61] A. Nogga, D. Hüber, H. Kamada, and W. Glöckle, Phys. Lett. **B409**, 19 (1997).
[62] H. Witała, W. Glöckle, J. Golak, A. Nogga, H. Kamada, R. Skibiński, and J. Kuroś-Żołnierczuk, Phys. Rev. C **63**, 024007 (2001).
[63] H. Witała, J. Golak, W. Glöckle, and H. Kamada, Phys. Rev. C **71**, 054001 (2005).
[64] H. Witała, J. Golak, R. Skibiński, W. Glöckle, W. N. Polyzou, and H. Kamada, Phys. Rev. C **77**, 034004 (2008).
[65] H. Kamada and W. Glöckle, Phys. Lett. **B655**, 119 (2007).
[66] St. Kistryn *et al.*, Phys. Lett. **B641**, 23 (2006).